Microstructure and Corrosion Properties of Friction Stir-Welded High-Strength Low -Alloy Steel

Amir Behjat[1] · Morteza Shamanian[1] · Masoud Atapour[1] · Mohammad Ahl Sarmadi[1]

Abstract The microstructure and corrosion behavior of friction stir (FS) welded API X-60 pipeline steel were investigated. Three FS welds were successfully fabricated under various welding conditions using a tungsten carbide-base tool. It was found that the microstructure and corrosion performance of the welds were strongly affected by welding parameters. A thermal history study of the welds showed that all stir zones heated up to the temperature of the ferrite–austenite region. Electron backscatter diffraction (EBSD) characterizations revealed that a significant grain refinement in the stir zones was accompanied by the formation of low angle grain boundaries. The kernel average misorientation analyses showed that the amount of residual strain and dislocation density were increased after welding. The corrosion assessments using potentiodynamic polarization and electrochemical impedance spectroscopy (EIS) measurements showed that the welds exhibited superior corrosion resistance than that of the base metal. There results were confirmed according to the immersion tests.

✉ Amir Behjat
  a.behjat@ma.iut.ac.ir

  Masoud Atapour
  m.atapour@cc.iut.ac.ir

[1] Department of Materials Engineering, Isfahan University of Technology, 84156-83111 Isfahan, Iran

1 Introduction

Demands for using high strength low alloy (HSLA) steels in ship building, automotive, pressure vessels and gas line pipes have continually increased in recent years [1–3]. HSLA steels exhibit a combination of high strength, ductility and good weldability. The presence of some micro-alloying elements (Vanadium, Titanium and Niobium) in these alloys can provoke a significant grain refinement and therefore enhance the strength-to-weight ratio and fracture toughness [3–5]. Generally, these alloys include a complex combination of ferrite, martensite and bainite.

Welding is an inevitable process for the manufacturing of many structures of HSLA steels. Traditional arc welding processes are the main techniques for joining of HSLA steels. However, the formation of a cast microstructure in the weld zone and grain growth in the heat affected zone can cause mechanical failures and limit the application of these steels [5–7]. For example, it has been reported that the occurrence of hydrogen induced cracking of arc welded structures of these steels can be due to grain coarsening in the HAZ [8, 9]

There are some investigations focused on the fusion welding of HSLA steels. For instance, Konkol et al. [9] reported that the fracture toughness of HSLA-65 steel was decreased after submerged arc welding. The liquation cracking susceptibility of HSLA-65 and HSLA-100 steels after fusion arc welding was investigated by Caron et al. [10]. They showed that the fusion boundary and HAZ suffered from grain coarsening. Based on the mentioned limitations of fusion welding, the investigations on the friction stir welding (FSW), which is a solid–state technique originally developed for difficult to weld Al-alloys [11–17], was increased for HSLA steels in these years [18–28]. Some studies were conducted on the materials

selection and design of tools for joining these hard metals [11, 21–28].

During the past years, a number of researchers investigated different aspects of HSLA welds fabricated by FSW process. Konkol et al. [20] reported that the mechanical properties of the FS welds of HSLA-65 were significantly superior in comparison with the welds made by submerged arc welding. They found that FSW was able to make a considerable grain refinement in the stir zone. In the work by Ozekcin et al. [21] on the FSW of an API-X60 steel, it was found that the grain size was strongly affected by heat input. Nelson et al. [24] reported that a hard area could be generated in the FS welds of HSLA-65 steel. Based on the thermal cycle examinations reported in [23] for FSW of a structural steel, it was found the microstructural and homogeneity of the welds were significantly affected by the peak temperature and cooling rate. In a recent work on FSW of HSLA-X65 [24], it was found that the cooling rate strongly changed the microstructure of the welds. Wei et al. [25] tried to improve the microstructure of a submerged arc weld of HSLA steels via FSW and showed that the generation of upper bainite phase was accelerated by increasing the tool rotational speed. A similar work by Nathan [26] showed that the formation of upper bainite was increased by increasing the shoulder diameter of the tool. The microstructural examinations by EBSD conducted by Ramesh et al. [27] confirmed the grain refinement during FSW of HSLA steels.

The present work was undertaken to evaluate the microstructural and corrosion properties of the FS welds of X-60 steel plate. The corrosion examination of the X-60 steel welds is an important work due to increase in the application of this steel in the oil, gas and sea water environments. To the best of our knowledge, this is the first work that systematically focuses on the corrosion behavior of this steel after FSW.

2 Materials and Methods

API X-60 pipeline steel with 3 mm thickness was used in this work. Table 1 shows the chemical composition of this base metal. Plates with dimensions of 120 mm in length and 40 mm in width were friction stir welded using WC/ 8 wt% Co tool, as shown in Fig. 1.

Single-pass butt joint procedure was carried out along the rolling direction of the plates. Before welding, the specimens were cleaned with sand grinding paper and degreased with methanol. The FSW parameters are presented in Table 2. In order to determine the thermal history during FSW, K-type thermocouples with a 0.5-mm diameter were placed in the center of the predicated stir zone (SZ), as shown schematically in Fig. 2. Microstructure of the welds was evaluated using optical microscopy (OM) and scanning electron microscopy (SEM). The samples were ground successively up to 2400 grit SiC abrasive papers and polished with 1 μm diamond paste to remove the rough weld surface. Finally, the specimens were etched using 2% Nital for 20 s and dried with cold air. EBSD examinations were carried out by a FE-SEM equipped with Oxford Instruments Channel 5 post processing software operated at 25 kV and the scan step size of 1 μm. Before EBSD, the surfaces were polished with 0.04 μm colloidal silica for 24 h in a vibro-meter.

For corrosion assessments, the specimens with a size of 5 mm × 5 mm were cut from the base metal and stir zone (SZ) of different welds. Prior to electrochemical tests, samples were ground using abrasive papers up to 1200 grits and then polished up to 1 μm diamond paste. A three-electrodes cell consisting of working electrode (base metal and SZ), a platinum as the counter electrode and Ag/AgCl saturated in KCl as the reference electrode was used for corrosion examinations. Before each corrosion tests, the specimens were immersed in open circuit potential for 1 h. All electrochemical tests were conducted using an Ivium potentiostat in 3.5 wt. % NaCl. Potentiodynamic polarization measurements were carried out using a scan rate of 1 mV/min from -250 mV to 500 mV with respect to OCP. The electrochemical impedance spectroscopy (EIS) measurements were performed at OCP over a scanning frequency ranging from 0.01 to 10,000 Hz and applied AC amplitude of 10 mV. All corrosion tests were repeated at least three times to examine the reproducibility.

The immersion tests were performed in 3.5 wt. % NaCl solution for 6 h to investigate the corrosion morphology and the extent of localized corrosion of the base metal and weld joints.

**Table 1** Nominal chemical composition of API 5L X-60 steel (wt.%)

Elements	C	V	Cr	Ni	S	P	Ti	Mo	Si	Mn	Fe
wt%	0.079	0.032	0.014	0.041	0.005	0.008	0.011	0.214	0.326	1.972	Balanced

Fig. 1 Tungsten carbide/
8wt%cobalt alloy friction stir
welding tool (all dimensions in
mm)
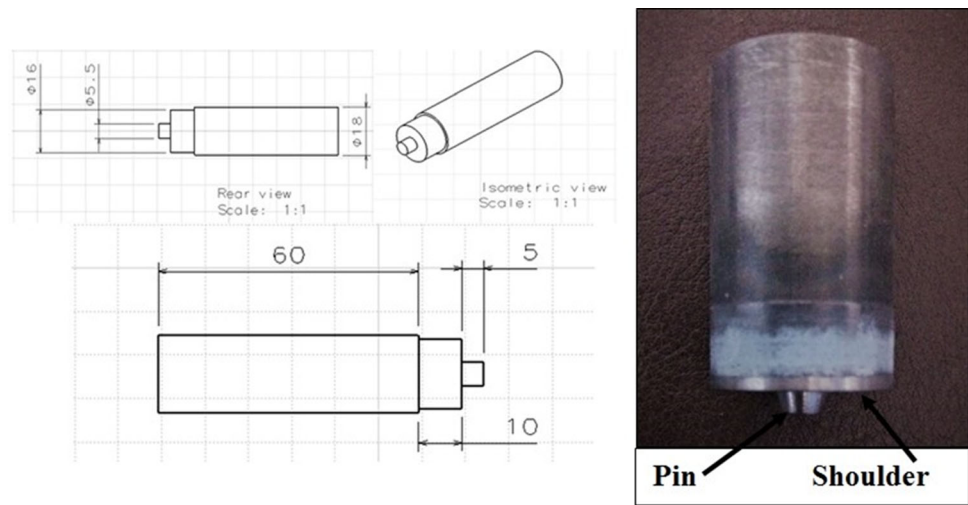
Table2 Friction stir welding parameters used in this work

No.	Transverse speed (mm/min)	Rotation speed (RPM)	Sample code	$\frac{v}{\omega}$(mm/rev)	Heat input(J/mm)
1	60	700	FSW 700–60	0.08	3850
2	40	1000	FSW 1000–40	0.04	5240
3	60	1000	FSW 1000–60	0.06	4430
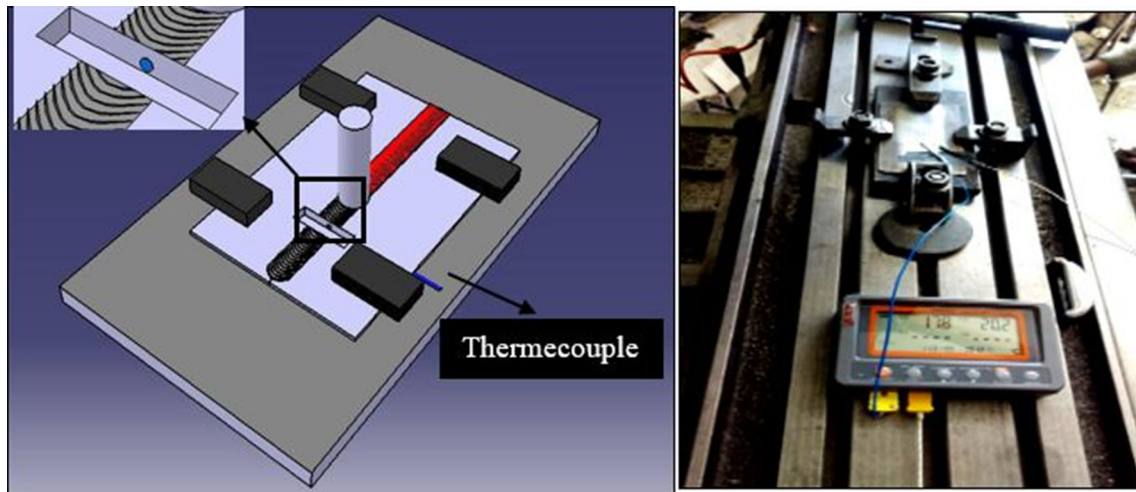
**Fig. 2 a** Schematic of FSW and **b** the location of thermocouple

3 Results and Discussion

3.1 Thermal Histories

Investigation of the temperature profile can be a powerful tool to determine the microstructure of the welds. Figure 3 shows the temperature profiles and the extracted data are presented in Fig. 3 and Table 3, respectively. It can be seen that the peak temperature was increased by increasing the tool rotation speed and decreasing the welding speed. Also,

it can be deduced that all the SZs experienced a temperature in austenite-ferrite dual-phase region (between Ac1 = 723 °C and Ac3 = 870 °C) [2]. Furthermore, the maximum heat input and the maximum cooling rate were recorded in the case of FSW 1000–40 and FSW 700–60, respectively. It is clear that the peak temperatures were lower than the transformation temperature of austenite to ferrite during FSW. In accordance with the literature [16–19], it can be seen that compared to the welding speed, the tool rotation speed exhibited stronger influence on the

Fig. 3 Thermal histories acquired from thermocouples placed near the bottom of stir zone
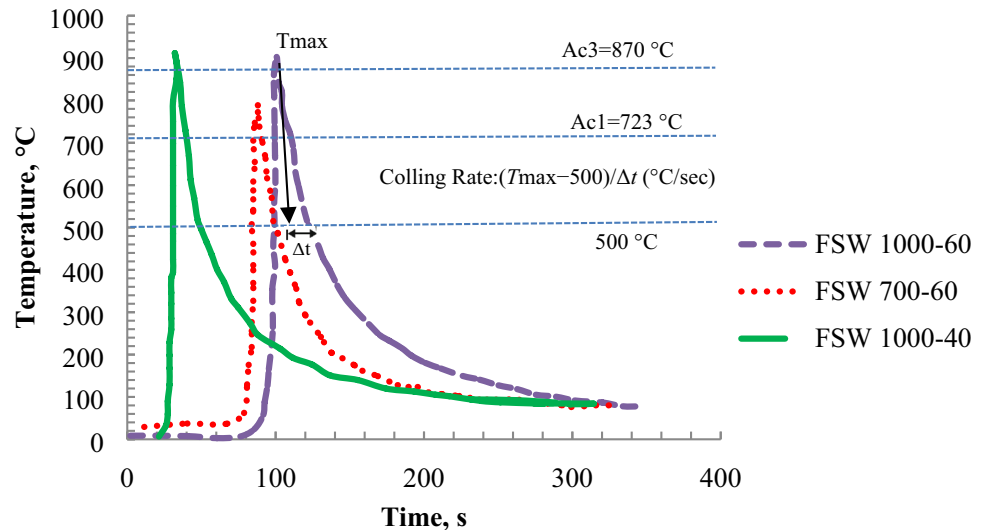
Table 3 Peak temperatures and cooling rates acquired from thermocouples

Sample code	$\frac{v}{\omega}$(mm/rev)	T_{max} (C°)	Cooling Rate $(T_{max} - 500)/ \Delta t$ (°C/sec)	Heat Input (J/mm)
FSW 700–60	0.08	788	21/5	3850
FSW 1000–40	0.04	911	12/4	5240
FSW 1000–60	0.06	893	18/2	4430

peak temperature. Also, the formation of different microstructures in the welds can be explained based on the differences in the temperature histories during FSW.

3.2 Microstructural Characterization

As shown in Fig. 4, the BM microstructure consists of pearlite islands randomly embedded in the polygonal fine-grained ferrite matrix. Some stretched grains are also observed in the BM due to the former rolling process. Figure 4c and d show the band contrast image and inverse pole figure (IPF) map, respectively. It can be seen that the ferrite grains with random orientation are present in the BM. Grain boundaries are displayed in different colors according to the defined grain boundary misorientation. Grain boundaries with misorientation between 5 to 15° are regarded as low-angle grain boundaries (LAGB). In contrast, the high-angle boundaries (HAGBs) are identified with misorientation of 15° or higher.

Figure 5 reveals the transverse macrostructure of the FSW 1000–40. As can be seen, the microstructure of the BM was completely disappeared after FSW. The SZ is primarily comprised of a fine mixed microstructure of ferrite and bainite as reported by several researchers in the case of HSLA steel welds [16–28]. Furthermore, it has

been reported that the partial or full reverse transformation to austenite can occur and then the transformation of austenite to ferrite and bainite during cooling will occur due to the induced strain during the FSW. Two microstructures of the HAZ were identified as the inner and outer HAZ (IHAZ and OHAZ, respectively). IHAZ exhibited a similar microstructure to the SZ. However, OHAZ had a temperature below the Ac1 and exhibited a very similar microstructure to that of the BM. No grain growth was observed in the OHAZ due to occurrence of a relatively low peak temperature during FSW process (below the ferrite–austenite two-phase region).

The results of EBSD examinations of the FSW 1000–40 weld are shown in Fig. 6. It is clear that the SZ is comprised predominantly of low angle grain boundaries. Also, FSW refined the microstructure of the BM in the SZ. According to the inverse pole figure (IPF) mapping in Fig. 6b, it can be deduced that a random texture occurred in SZ.

The results of the grain boundary misorientation and grain size distribution measurements are illustrated in Fig. 7. A homogenous distribution of both low and high angle boundaries is evident for the BM (Fig. 7a). According to Fig. 7c, the fraction of low angle boundaries (low misorientation) was higher at the SZ compare to that
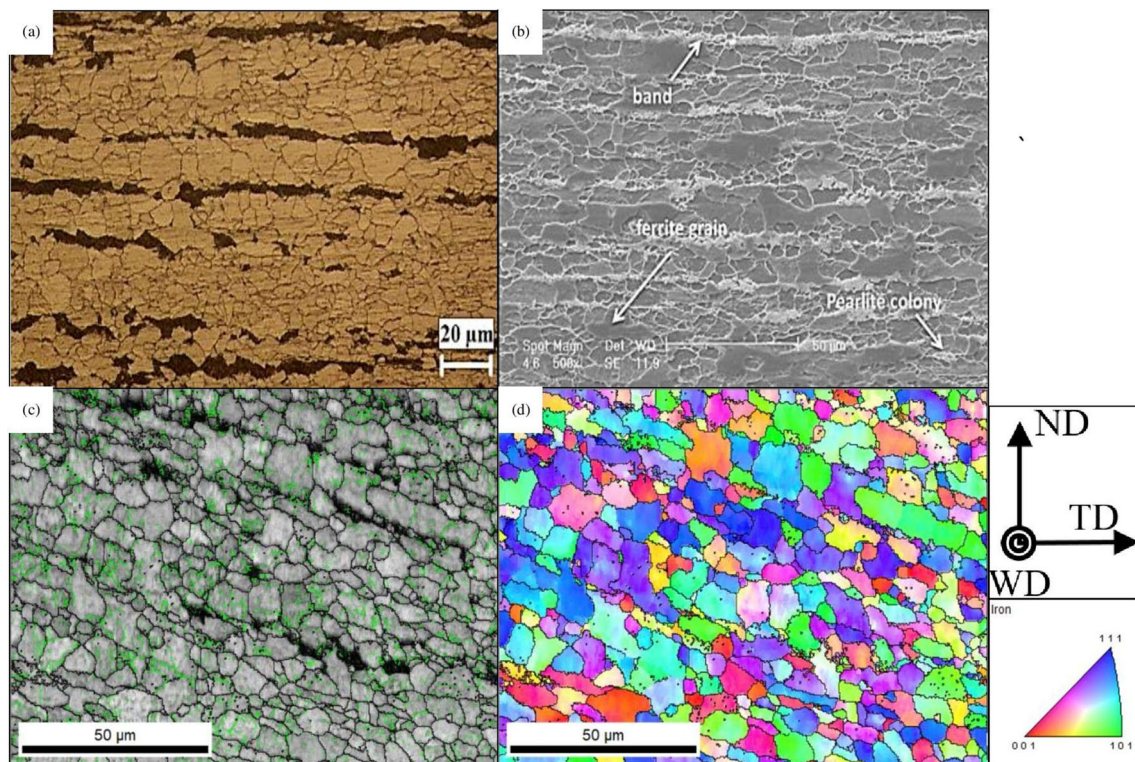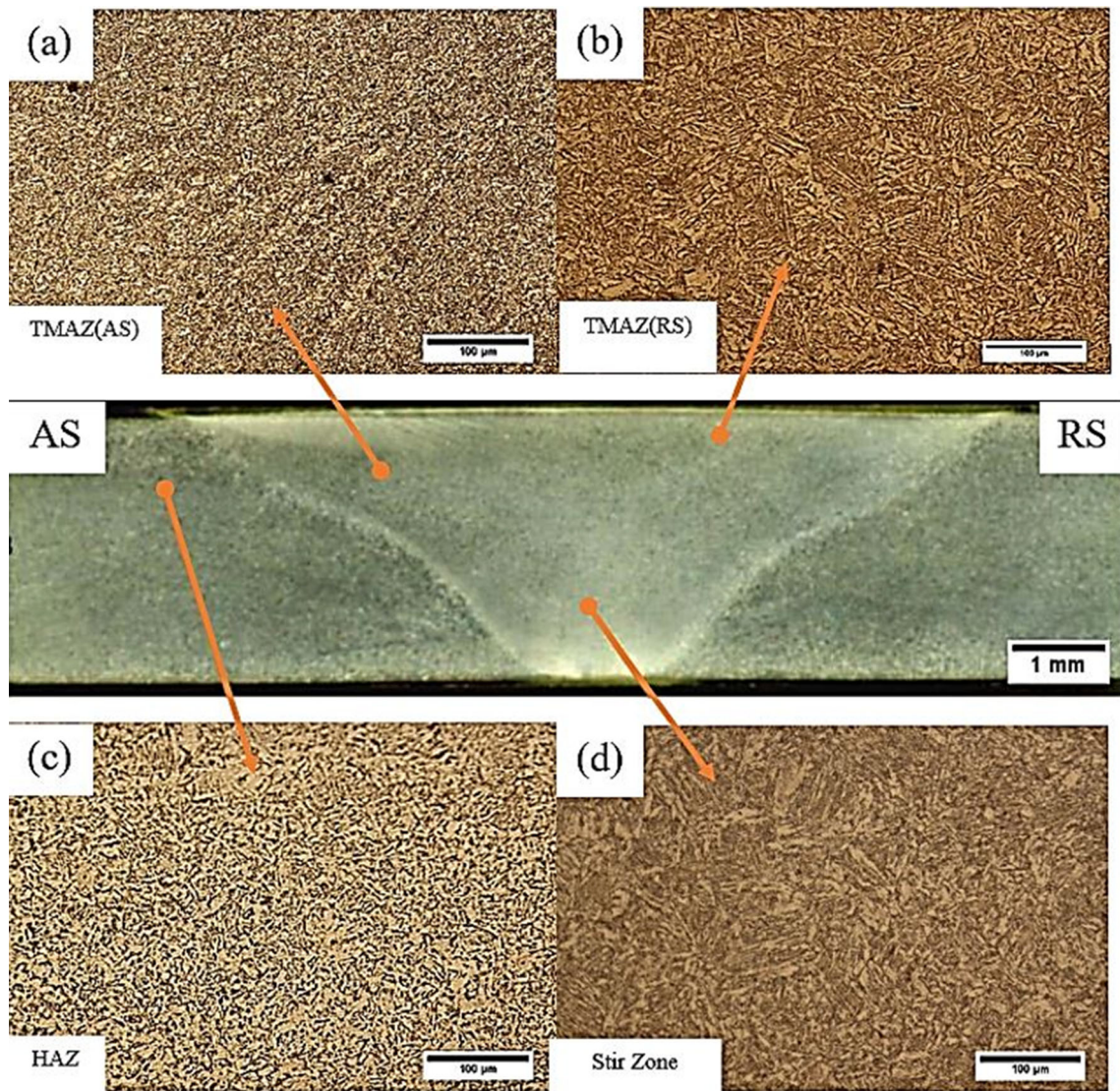
Fig. 4 Microstructure of the base metal: **a** optical micrograph, **b** SEM micrograph, **c** image quality with imposed grain boundaries and **d** inverse pole figure map at the surface of ND-TD plane

observed at the BM. Some of grains were deformed during FSW and full recrystallization was not possible. Also, more density of high angle boundaries and grain refinement were seen in SZ compared to BM. The average grain size was determined to be 10 ± 1 μm and 3 ± 2 μm for the BM and SZ, respectively.

Kernel average misorientation maps (KAM) and kernel average degrees are shown in Fig. 8. KAM shows an average misorientation between a given point and its neighbors inside the grains. It is considered as a measure of dislocation density and can be used to correlate plastic deformation to the misorientation within the microstructure. The misorientation in the BM and SZ was determined as 0.8° and 1.3°, respectively. Higher local misorientation within grains corresponds to higher dislocation densities. In other words, it can be concluded the full recrystallization was not achieved during welding due to the presence of high dislocation density in the weld. It is well demonstrated that the amount of heat generated during welding (welding heat input) is a key factor affecting the microstructure, mechanical and corrosion behavior of the welds [12–15]. The heat input is controlled by welding parameters such as transverse speed and tool rotation speed or the heat input. In addition, the microstructure in different weld regions is strongly dependent on the peak temperature, cooling rate and strain rate [15–19].

The optical microstructure of three welds is shown in Fig. 9. Various morphologies of polygonal ferrite represented as (α), Widmanstatten ferrite (α_w) and bainite (α_b) were observed in the SZ of all welds. This confirms that the microstructure of the welds is controlled by the amount of heat input and cooling rate. Also, this difference in microstructure can be attributed to the amount of stress and strain generated in the material during process. Several authors proposed that the bainite formation is suppressed when the austenite grains experience severe deformation upon cooling. Also, it has been reported that increase in nucleation sites and dislocation density is associated with the formation of ferrite [25–29]. A bainite/Widmanstatten ferrite microstructure was formed in the weld fabricated at lower travel speed (40 mm/min) (Fig. 9a). However, bainite/Widmanstatten ferrite grains were formed in the weld obtained at a higher travel speed of 60 mm/min. As illustrated in Fig. 9b, it seems high driving force for recrystallization for the weld obtained at high travel speed led to the formation of a fine bainite/Widmanstatten ferrite structure.

Figure 9c reveals that a considerable quantity of ferrite was formed in the SZ of the weld fabricated at a high transverse speed (60 mm/min) and low rotation speed (700 rpm). As reported by others [12–18], this can be

Fig. 5 Optical micrographs of weld cross section FSW 1000–40 **a** advancing side, **b** retreating side, **c** heat affected zone, **d** stir zone
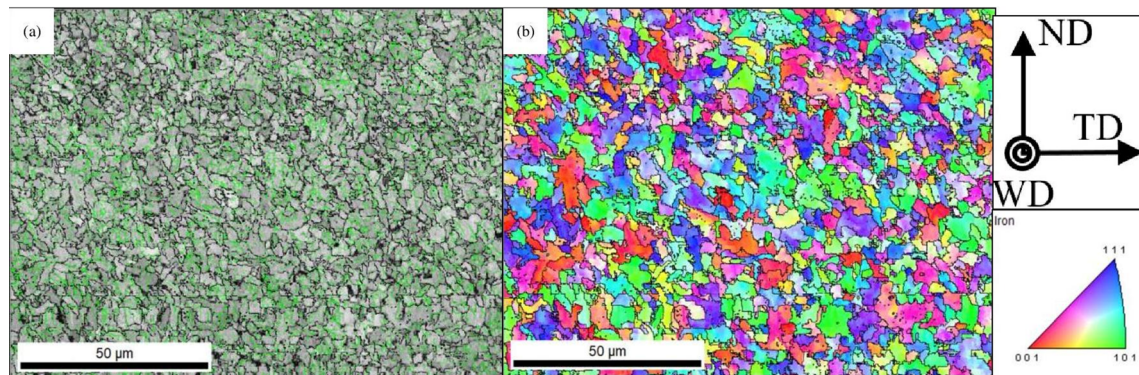
Fig. 6 Microstructure of weld stir zone of FSW 1000–40 **a** image quality with imposed grain boundaries and **b** inverse pole figure map at the surface of ND-TD plane
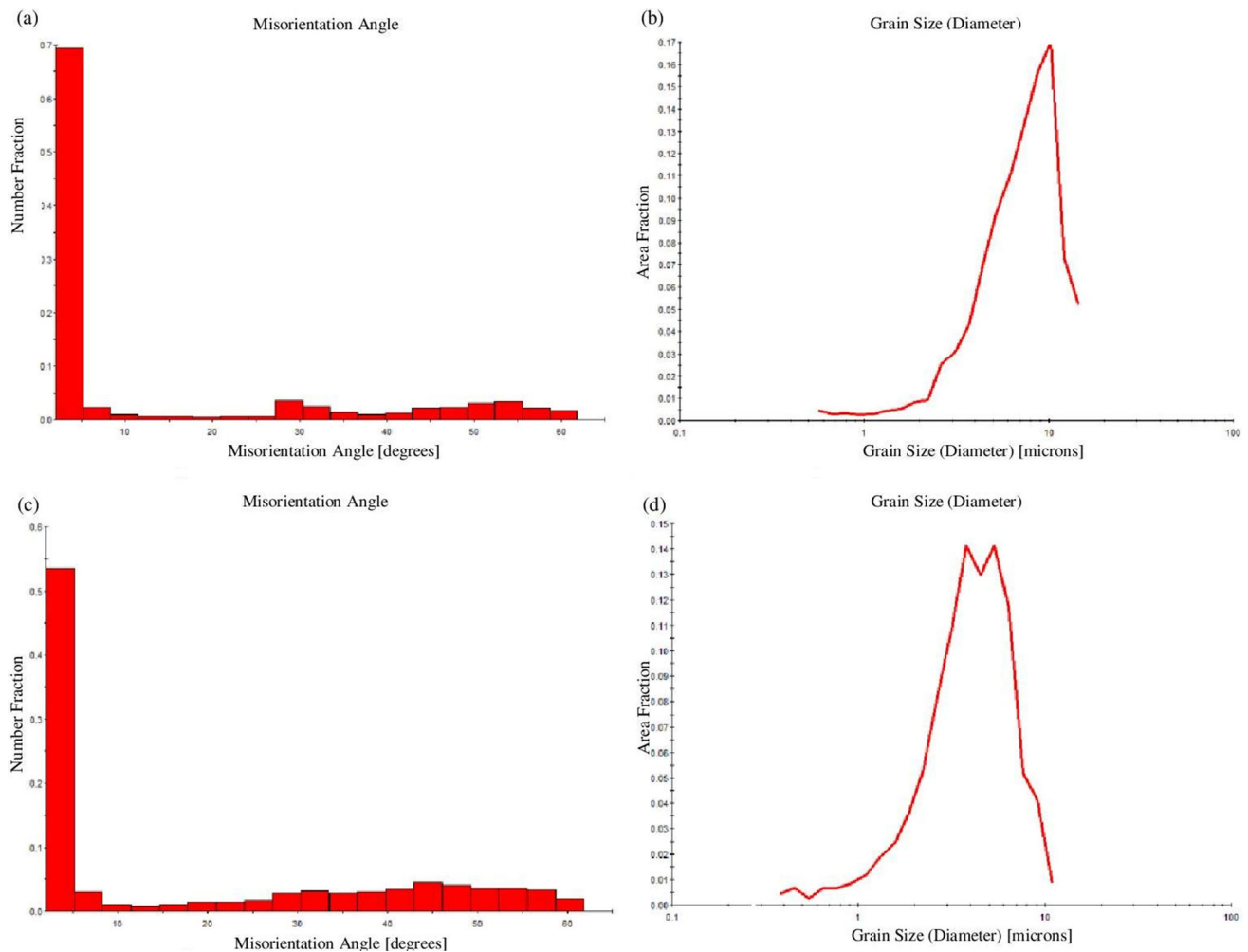
Fig. 7 Grain boundary misorientation and grain size distribution in (a,b) base metal (c,d) stir zone, respectively

attributed to the special mechanical cycle that occurred during FSW in these conditions.

3.3 Corrosion studies

3.3.1 Open Circuit Potential Measurements

The corrosion behavior of the welds has been investigated using OCP, EIS, polarizations and immersion evaluations in 3.5% NaCl electrolyte. The OCP of all the tested specimens showed a reducing trend during 3600 s of immersion time (Fig. 10). Decrease in the corrosion potential can be related to the dissolution and development of corrosion products on the surface of the specimens [30–32]. It should be noted that the BM exhibited the lowest OCP. It means the welds showed a superior stability than the BM in 3.5% NaCl. This behavior can be related to the grain refinement and change in the microstructure after FSW. Also, comparison of the various weld samples showed that FSW specimen with higher heat input (FSW1000-40) had the

lowest OCP, which attributed to the different behavior of dissolution of preformed air oxide film, thickening of the formed oxide layer and formation of corrosion products on the surface of the specimens.

3.3.2 Potentiodynamic Polarization Measurements

The potentiodynamic polarization curves obtained after 1 h immersion at OCP are presented at Fig. 11. As reported by other authors, HSLA steels suffer from different corrosion types like uniform, localized and galvanic corrosion in 3.5% NaCl electrolyte [30–34]. The corrosion current density and corrosion potentials were extracted from the polarization curves and summarized in Table 4. As seen, the SZ exhibited superior corrosion potential than the BM. These results are in a good agreement with previous works [36, 37]. However, it can be deduced that the corrosion rate of the welds was independent of the welding parameters.
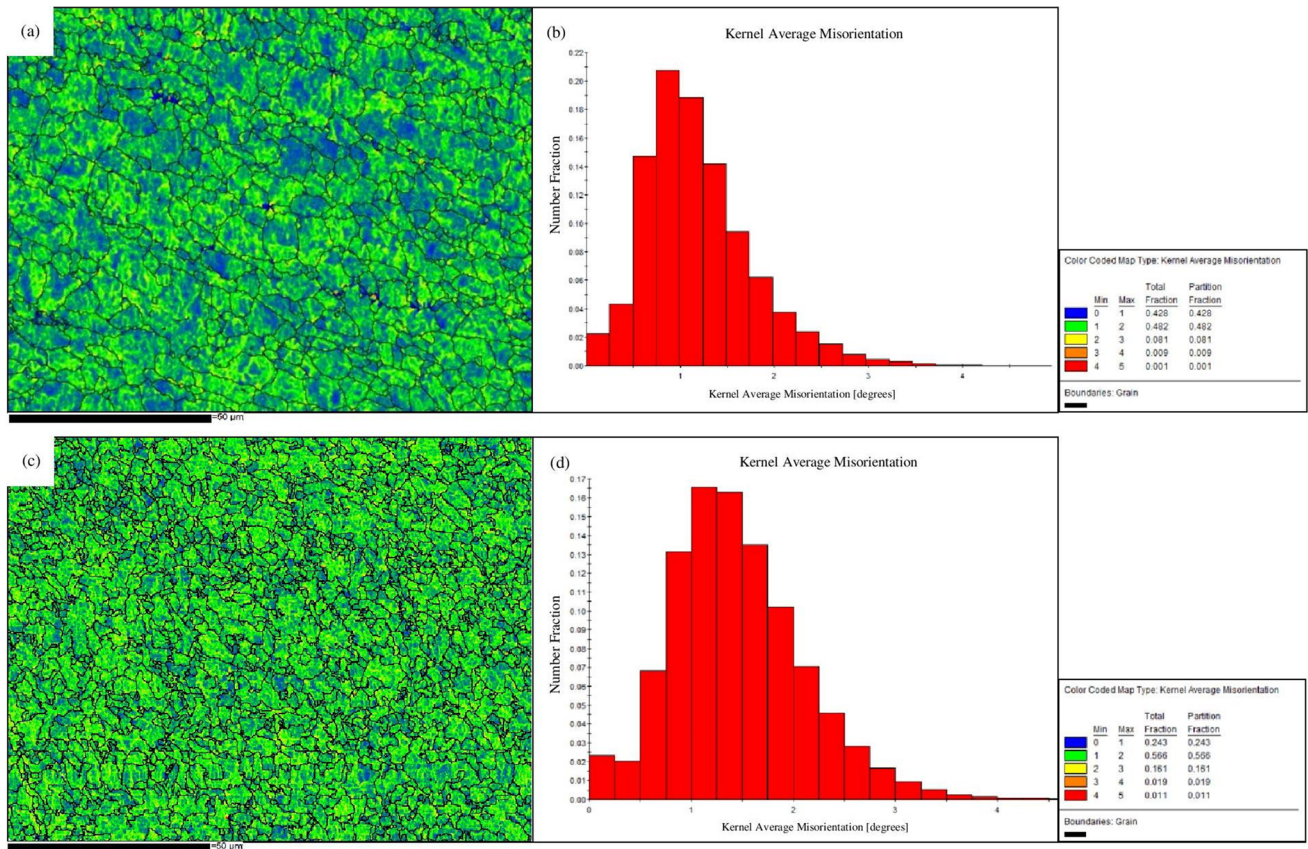
Fig. 8 Kernel Average Misorientation map and Kernel Average Misorientation degree versus relative frequency at surface of RD-TD planes in (**a**, **b**) base metal (**c**, **d**) stir zone, respectively

3.3.3 Electrochemical Impedance Spectroscopy (EIS) Measurements

EIS is an important technique for understanding the mechanism of the corrosion [38–42]. Typical Nyqusit diagrams of the BM and SZ specimens are depicted in Fig. 12. All Nyquist plots revealed a single arc, which is associated with charge transfer resistance and a large arc diameter usually meant better corrosion resistance [40–43]. Therefore, the corrosion resistance and electrochemical reaction inhibition of SZ were better than BM. This result agrees well with the obtained data by polarization measurements.

3.3.4 Immersion Test

In order to obtain more details on the corrosion aspects of the welds, the immersion tests were conducted in 3.5% NaCl solution for 6 h. As shown in Fig. 13, the level of corroded area decreased after welding by FSW. The formation of some large corroded area in the BM can be related to the high deriving force of galvanic corrosion due to the presence of the coarse microstructure and ferrite/pearlite structure. As reported by others [36–40], the galvanic corrosion is one of the main corrosion mechanisms in the welds and the grain refinement in the FS welds decreased the galvanic corrosion. In HSLA steels, corrosion takes place predominantly by the formation of local galvanic cells between ferrite and cementite phases [33–35]. It seems a uniform distribution of cementite particles in the ferrite matrix (SZ microstructure) led to decreasing the dissolution of anodes (ferrite). Compared to the BM, shallow attacks and uniform corrosion on ferrite regions were observed in the SZs. This behavior can be related to the decrease in the galvanic corrosion in the SZs [35–37]. Briefly, the severity of attack in the ferrite region of pearlite (BM) was higher than that observed for the ferrite in bainite structure (SZ).

4 Conclusions

The microstructural and corrosion properties of FSW of X-60 steel plate were investigated. The main conclusions can be summarized as follows:
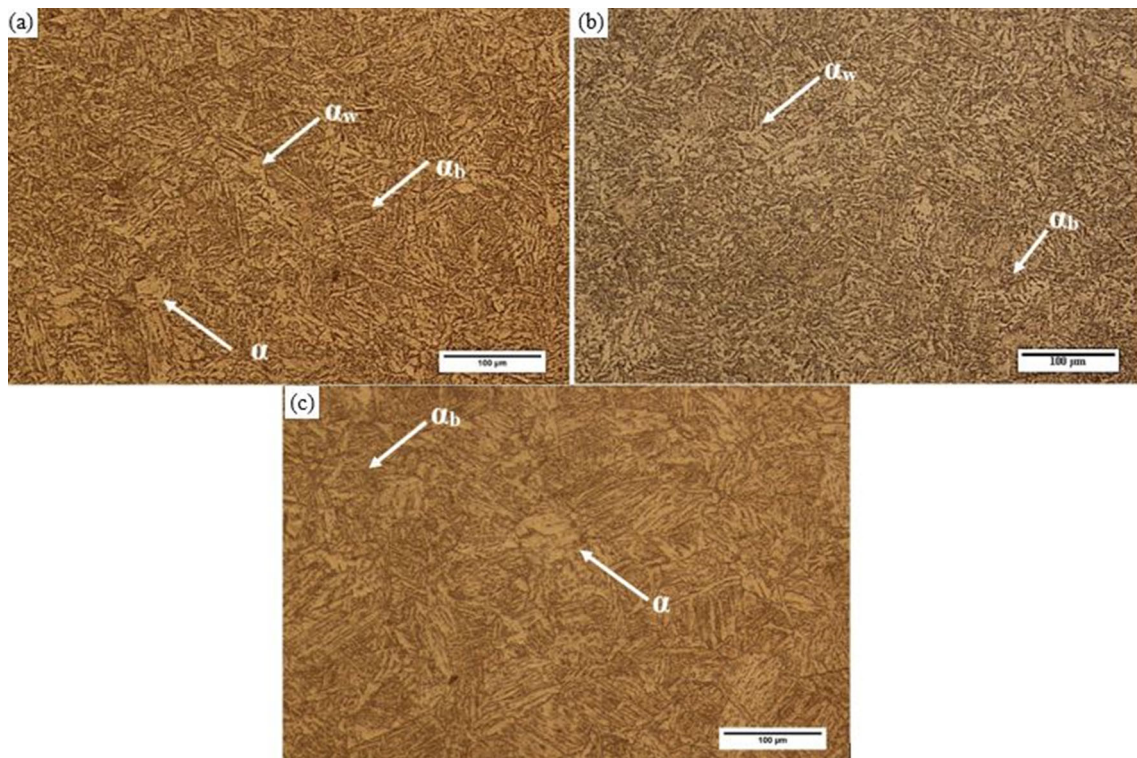
Fig. 9 Microstructures of weld stir zone (SZ) at various heat inputs, **a** 1000 rpm 40 mm/min, **b** 1000 rpm 60 mm/min, **c** 700 rpm 60 mm/min (α = Ferrite, α_b = Bainite, α_w = Widmanstatten ferrite)

Fig. 10 Open circuit potential curves of base metal and various FS welds in 3.5% NaCl
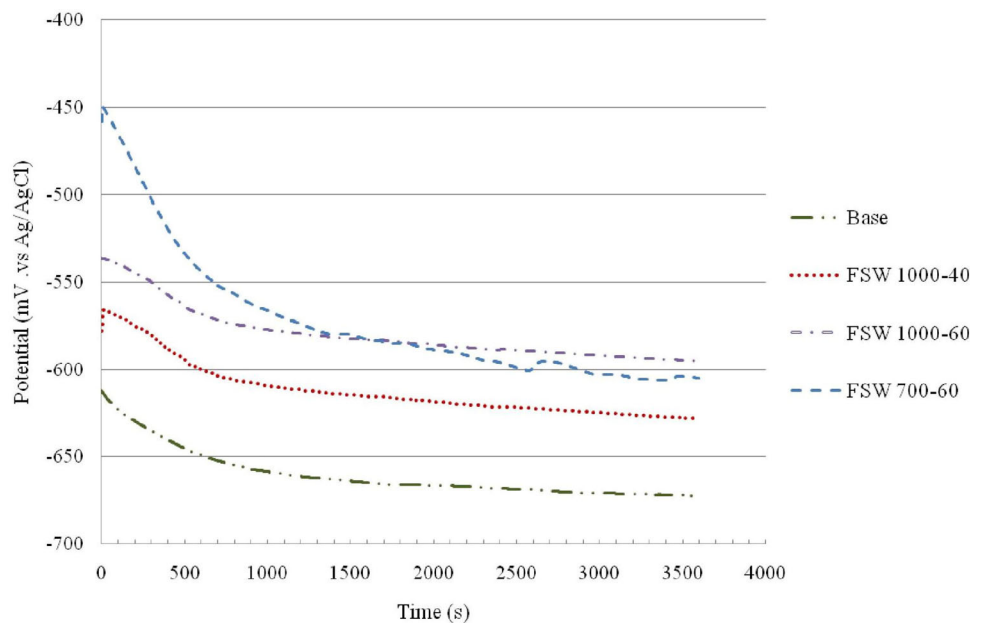
- The thermal history diagrams revealed that all stir zones heated up to the temperature of the ferrite–austenite region.
- All the SZs showed the various morphologies of polygonal ferrite represented as (α), Widmanstatten ferrite (α_w) and bainite (α_b) microstructure.

- The EBSD characterizations revealed that the grain size was finer in the SZ of the weld compared to the BM. Also, SZ exhibited higher density of low angle grain boundaries.
- The KAM maps of the welds demonstrated that the deformation was more concentrated in the SZ. It means

Fig. 11 Potentiodynamic polarization curves of base metal and various FS welds in 3.5% NaCl
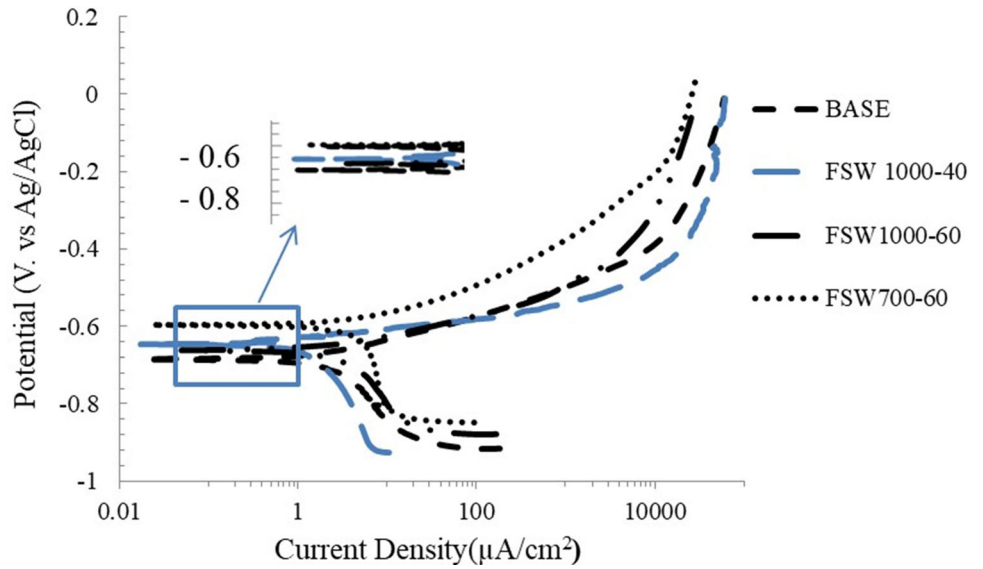

Table 4 Summary of OCP and potentiodynamic polarization results in 3.5% NaCl

Sample code	$E_{ocp}(V)$	$E_{corr}(V)$	$I_{corr}(\mu A/cm^2)$	Corrosion rate (mm/year)	Heat input (J/mm)
Base metal	− 0.661 ± 0.008	− 0.688 ± 0.008	11.84 ± 0.14	0.14 ± 0.02	–
FSW 700–60	− 0.608 ± 0.006	− 0.620 ± 0.006	12.84 ± 0.23	0.15 ± 0.03	3850
FSW 1000–40	− 0.630 ± 0.005	− 0.652 ± 0.005	11.74 ± 0.17	0.15 ± 0.02	5240
FSW 1000–60	− 0.593 ± 0.007	− 0.664 ± 0.007	12.64 ± 0.15	0.14 ± 0.04	4430

Fig. 12 EIS Nyquist plots of base metal and various FS welds in 3.5% NaCl
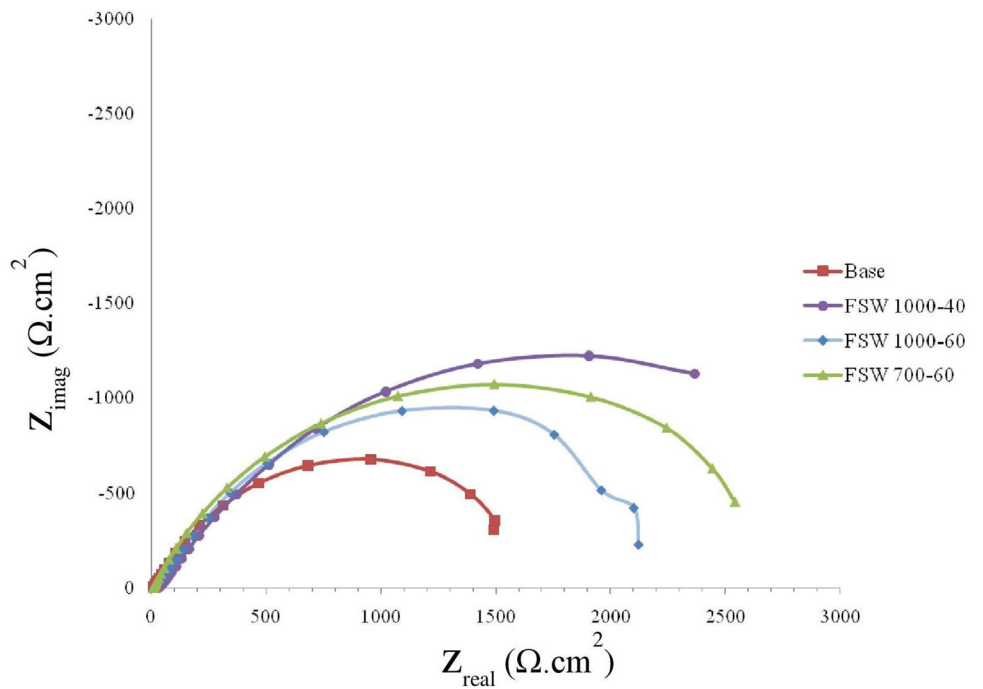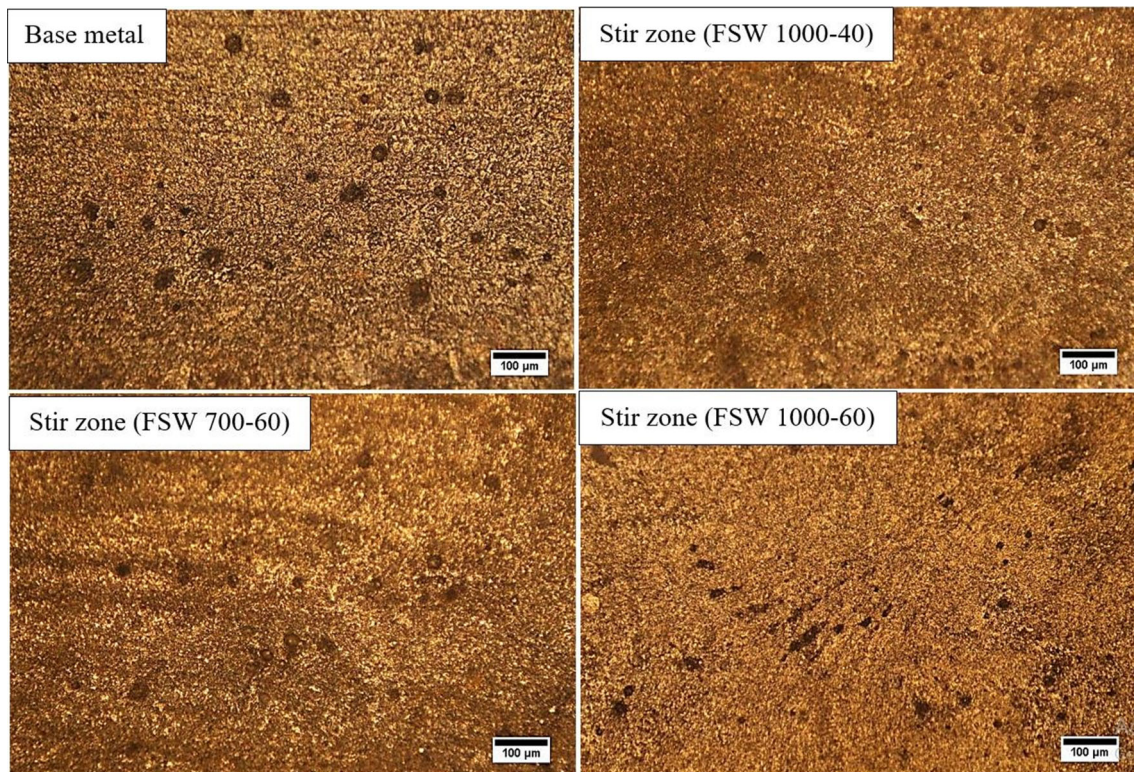
Fig. 13 Optical micrographs of corrosion morphology of the base metal and different FS welds after immersion test in 3.5% NaCl solution for 6 h

that the dislocation density and residual stress were higher in the SZ than those in the BM.

- The results of the polarization, EIS and immersion tests showed that the corrosion performance of HSLA steel was improved after FSW.

References

[1] Sampath K, *J Mater Eng Perform* **15** (2006) 32.
[2] Davis J R, *ASM Internatinal* **17** (2001) 193.
[3] Sha W, *Springer* (2013).
[4] Show B K, Veerababu R, Balamuralikrishnan R, Malakondaiah G, *Mater Sci Eng A* **527** (2010) 1595.
[5] Hong S, Kang K, Park C, *Scripta Materialia* **46** (2002) 163.
[6] Sun W, Wang G, Zhang J, Xia D, Sun H, *J Mater Sci Technol* **25** (2009) 857.
[7] Yayla P, Kaluc E, Ural K, *Mater Des* **28** (2007) 1898.
[8] Kang J, Wang C, Wang G, *Mater Sci Eng A* **553** (2012) 96.
[9] Konkol P, Warren J, *Welding Journal* **77** (1998) 361.
[10] Caron J, Babu S, Lippold J, *Welding Journal* **92** (2013) 110.
[11] Mishra R S, Kumar N, *Springer* (2014).
[12] Kumar K, Kalyan C, *Mater Manuf Proces* **24** (2009) 438.
[13] Lienert T, Stellwag W, *Welding Journal* **82** (2003) 1.
[14] Pradeep A, *Inter J of Eng Research Develop* **3** (2012) 75.
[15] McPherson N, Galloway A, Cater S, Hambling S, *Sci Technol of Weld Join* **18** (2013) 441.

[16] Barnes S, Bhatti A, Steuwer A, Johnson R, Altenkirch J, Withers P, *Metall and Maters Trans A* **43** (2012) 2342.
[17] Sunilkumar D, Muthukumaran S, *Trans Indian Inst Met* **72** (2019) 1537.
[18] Baker T N, McPherson N A, *J Mater Sci Techn* **32** (2016) 234.
[19] Mironov S, Sato Y, Kokawa H, *Acta Materialia* **56** (2008) 2606.
[20] Konkol P J, Mruczek M F, *Welding Journal* **86** (2007) 187.
[21] Ozekcin A, Jin H, *Inter J of Offshore and Polar Eng* **14** (2004) 284.
[22] Ragu Nathan S, Balasubramanian V, *Trans Indian Inst Met* **69** (2016) 1861.
[23] Ghosh M, Kumar K, Mishra R, *Mater Sci Eng A* **528** (2011) 8111.
[24] Nelson T W, Rose S A, *J Mater Process Technol* **231** (2016) 66.
[25] Wei L, Nelson T W, *Mater Sci Eng A* **556** (2012) 51.
[26] Nathan S R, Balasubramanian V, Malarvizhi S, Rao A, *Defense Technol* **11** (2015) 307.
[27] Ramesh R, Dinaharan I, Kumar R, Akinlabi E, *Mater Sci Eng A* **687** (2017) 39.
[28] Abbasi M, Nelson T W, *Mater Character* **66** (2012) 1.
[29] Bhadeshia H, Honeycombe R, *Butterworth-Heinemann* (2011).
[30] Wang Z, Li P, Guan Y, Chen Q, Pu S, *Corr Sci* **51** (2009) 954.
[31] Chen Y, Tzeng H, Wei L, Wang L, Oung J, Shih H, *Corr Sci* **47** (2005) 1001.
[32] Guo J, Yang S, Shang C, Wang Y, He X, *Corr Sci* **51** (2009) 242.
[33] Moon A, Sangal S, Layek S, Giribaskar S, Mondal K, *Metall and Maters Transs A* **46** (2015) 1500.
[34] Kumar V, Chaudhuri S K, *Corr Reviews* **21** (2003) 293.
[35] Lakshmana R B, Chaudhari P, Nath S, *Mater and Des* **32** (2011) 433.
[36] Abbaszadeh K, Saghafian H, *J Mater Sci Tech* **28** (2012) 236.

[37] Trinh D, Frappart S, Ruckert G, Cortial F, Touzain S, *Corr Eng Sci Technol* **54** (2019) 353.

[38] Rajesh S, Vishvesh B, *Mater and Manufact Process* **33** (2018) 156.

[39] Sarlak H, Atapour M, Esmailzadeh M, *Mater and Des* **66** (2015) 209.

[40] Navaser M, Atapour M, *J Mater Sci Techno* **33** (2017) 155.

[41] Atapour M, Pilchak A L, Frankel G S, Williams J C, *Metall Mater Trans A* **41** (2010) 2318.

[42] Seikh A, Sherif E, *Int J. Electrochem. Sci* **10** (2015) 895.

[43] Guo Y, Li C, Liu Y, Yu L, *Int J Min, Met Mater* **22** (2015) 604.

Publisher's Note Springer Nature remains neutral with regard to jurisdictional claims in published maps and institutional affiliations.